Crystallize it before it diffuses: Kinetic stabilization of thin-film phosphorus-rich semiconductor CuP_2

Andrea Crovetto,[*,†,‡] Danny Kojda,[¶] Feng Yi,[§] Karen N. Heinselman,[†] David A. LaVan,[§] Klaus Habicht,[¶,‖] Thomas Unold,[‡] and Andriy Zakutayev[*,†]

†*Materials Science Center, National Renewable Energy Laboratory, Golden, Colorado 80401, United States*

‡*Department of Structure and Dynamics of Energy Materials, Helmholtz-Zentrum Berlin für Materialien und Energie GmbH, 14109 Berlin, Germany*

¶*Department Dynamics and Transport in Quantum Materials, Helmholtz-Zentrum Berlin für Materialien und Energie GmbH, 14109 Berlin, Germany*

§*National Institute of Standards and Technology, Material Measurement Laboratory, Gaithersburg, Maryland 20899, United States*

‖*Institute of Physics and Astronomy, University of Potsdam, 14476 Potsdam, Germany*

E-mail: Email:ancro@dtu.dk; Email:andriy.zakutayev@nrel.gov

Abstract

Numerous phosphorus-rich metal phosphides containing both P-P bonds and metal-P bonds are known from the solid-state chemistry literature. A method to grow these materials in thin-film form would be desirable, since thin films are required in many applications and they are an ideal platform for high-throughput studies. In addition, the high density and smooth surfaces achievable in thin films are a significant advantage for characterization of transport and optical properties. Despite these benefits, there is hardly any published work on even the simplest binary phosphorus-rich phosphide films. Here, we demonstrate growth of single-phase CuP_2 films by a two-step process involving reactive sputtering of amorphous CuP_{2+x} and rapid annealing in an inert atmosphere. At the crystallization temperature, CuP_2 tends to decompose into Cu_3P and gaseous phosphorus. However, CuP_2 can still be synthesized if the amorphous precursors are mixed on the atomic scale and are sufficiently close to the desired composition (neither too P poor nor too P rich). Fast formation of polycrystalline CuP_2, combined with a short annealing time, makes it possible to bypass the diffusion processes responsible for decomposition. We find that thin-film CuP_2 is a 1.5 eV band gap semiconductor with interesting properties, such as a high optical absorption coefficient (above $10^5\,\mathrm{cm}^{-1}$), low thermal conductivity (1.1 W/Km), and composition-insensitive electrical conductivity (around 1 S/cm). We anticipate that our processing route can be extended to other phosphorus-rich phosphides that are still awaiting thin-film synthesis, and will lead to more complete understanding of these materials and of their potential applications.

Introduction

Phosphorus readily forms homoelement bonds in the solid state. Accordingly, over a hundred phosphorus-rich binary metal phosphides containing both P-P bonds and metal-P bonds have been synthesized in bulk form.[1,2] Often, these compounds have semiconducting properties and decompose into elemental phosphorus and a metal-rich phosphide (with only metal-P bonds) at high temperatures.[2] Thin-film synthesis of P-rich materials would help determine their technological potential and their compatibility with established materials and processes. In addition, growing these materials in thin-film form would be desirable for high-throughput characterization of their properties as a function of composition and process conditions. However, reports of polycrystalline P-rich phosphides as thin films are very scarce and seem to be limited to basic characterization of ZnP_2 and CdP_2 deposited by evaporation of powders of the pre-synthesized compounds.[3,4] Thin-film growth from elemental or gaseous sources would significantly simplify the synthesis process. However, the high P partial pressure required to stabilize these P-rich compounds poses additional challenges for thin-film synthesis with respect to bulk synthesis. The classic synthesis method of heating the elements in powder form in a sealed ampoule cannot easily be extended to phosphorization of metal thin films. Since the volume of a thin film is very small, it is difficult to achieve a sufficiently high P partial pressure without excessive P recondensation on the film. On the other hand, open-system processes with fixed gas flow rates are more controllable, but the combination of a high P partial pressure, high temperature, and a continuously flowing P source requires careful safety measures.

Similar to other P-rich phosphides, bulk synthesis of CuP_2 as a single-crystal or powder is well established[5–10] but there are no reports of thin-film growth. CuP_2 is a semiconductor that has been proposed as a solar absorber,[11] thermoelectric material,[12,13] electrocatalyst for hydrogen- and oxygen evolution,[14] and as a component in composite anode materials for Li-[15–17] and Na-based batteries.[18,19] Although CuP_2 has been incorporated in electrochemical devices, its optoelectronic and thermoelectric characterization is incomplete. For example, the optical absorption coefficient of CuP_2 crystals has only been measured in the weak absorption region just above its 1.4 eV–1.5 eV band gap,[8,10] so it is impossible to evaluate its performance as a light absorber in the visible. For thermoelectric applications, the properties needed to calculate the quality factor zT have only been measured separately on different CuP_2 specimens in single-crystal or powder form. A potential method for growing phosphorus-rich phosphide thin films is reactive sputtering. We have recently shown the feasibility of this deposition technique for various metal-rich phosphide compounds.[20–22]

In this work, we present a relatively simple two-step process route to grow polycrystalline CuP_2 thin films as semiconductors of potential technological interest. First, we reactively sputter amorphous CuP_{2+x} in a PH_3-containing atmosphere. The advantage of this process

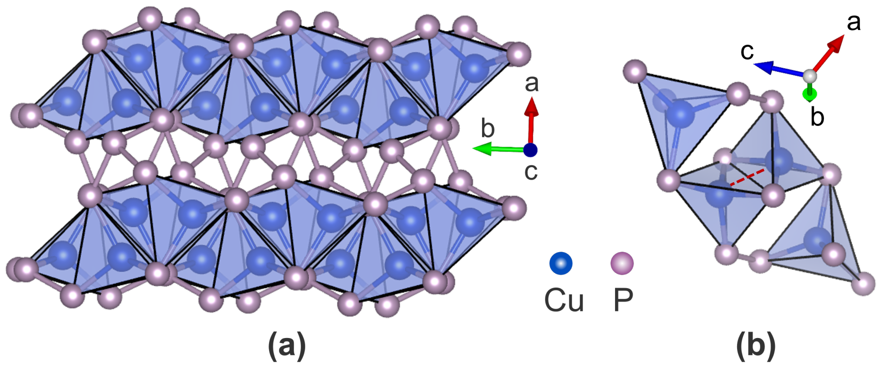

Figure 1: The monoclinic P2$_1$/c structure of CuP_2. (a): View emphasizing the sheets of CuP_4 tetrahedra and of single-bonded P atoms. (b): View emphasizing the short Cu-Cu distance (dashed line) between two edge-sharing CuP_4 tetrahedra.[23]

step is that sufficient P can be incorporated in the films at room temperature at a relatively low PH_3 partial pressure (0.1 Pa). In the second step, we crystallize the CuP_{2+x} films by rapid thermal annealing (RTA) at atmospheric pressure under an inert gas flow. With this two-step process, high phosphorus partial pressures at high temperatures are avoided. We find that the crystallization step must be kinetically facilitated by employing amorphous precursors of sufficiently similar composition to the desired CuP_2 stoichiometry. We investigate the optical properties of CuP_2 over a broad spectral range and conduct comprehensive temperature -dependent thermoelectric characterization (including the zT value) up to room temperature. We find a remarkably high optical absorption coefficient (above $10^5\,\mathrm{cm}^{-1}$ in the visible), low thermal conductivity (1.1 W/Km), composition-insensitive electrical conductivity (1 S/cm) and a moderate native doping density ($10^{15}\,\mathrm{cm}^{-3}$–$10^{17}\,\mathrm{cm}^{-3}$) potentially suitable for photovoltaic applications.

Results and discussion

Structure and bonding

Bonding in CuP_2 has some interesting features that are worth a brief analysis. Bulk CuP_2 crystallizes in the monoclinic structure shown in Fig. 1, with space group P2$_1$/c.[7] The structure consists of alternating sheets of CuP_4 tetrahedra and of homoelement-bonded P atoms in planes parallel to (100) (Fig. 1). Each CuP_4 tetrahedron shares an edge and three corners with other analogous tetrahedra. The existence of anion-anion bonding is a key qualitative difference between P-rich compounds like CuP_2 and most optoelectronic compounds such as III-V and II-VI semiconductors. The generalized $8 - N$ rule[24] can then be used to interpret bonding. In this framework, one may assign the -1 oxidation state to one half of the P atoms, since they are bonded to two other P atoms and three Cu atoms. The remaining P atoms have three P-P bonds and one Cu-P bond and are formally neutral, as the three homoelement bonds complete their octet. To achieve charge neutrality, Cu should then be in the $+1$ oxidation state. While explicit calculations[12] indicate that only about 30% of this charge is actually transferred to P due to significant covalency, they also confirm that the charge is only accepted by the P atoms that are in the -1 oxidation state. Thus, CuP_2 is a relatively rare example of a compound with mixed anion valence.

Another peculiar feature of the $P2_1/c$ structure of CuP_2 is that pairs of Cu atoms are quite close to each other (2.48 Å).[7] Comparing this distance to the bond length of metallic Cu (2.55 Å) and the metallic radius of single-bonded Cu (2.49 Å)[25] suggests that some metallic Cu-Cu bonding is to be expected. This is confirmed by calculation of a non-zero electron localization function between the two Cu atoms and by experimental analysis of phonon modes in CuP_2.[26] These Cu-Cu dimers were recently shown to vibrate anharmonically as a rattling mode and strongly scatter acoustic phonons.[26] This is the key feature enabling low lattice thermal conductivity in CuP_2 in spite of its relatively high acoustic conductivity, thus making it interesting for thermoelectrics.

Synthesizability

CuP_{2+x} thin films with a broad range of x (positive and negative) could be deposited by reactive sputtering in a PH_3/Ar atmosphere at room temperature, using either a Cu target, a Cu_3P target, or both at the same time (see the Experimental Details and the x-axis in

Fig. 2(a)). The main available parameters to tune x are the RF power on the targets and the PH_3 partial pressure (see Supporting Information). Decreasing the power led to higher P contents due to a more P-enriched target surface and/or to a lower flux of Cu at the substrate, promoting phosphorization at the substrate. Higher PH_3 partial pressures can be achieved by increasing the total pressure or the PH_3 concentration in Ar. Because the PH_3 concentration was limited to below 5% in our setup, we had to employ a relatively high sputter pressure ($2\,\mathrm{Pa} \simeq 15\,\mathrm{mTorr}$) to obtain films of CuP_2 stoichiometry. The wide tunability of the P content in Cu-P films was also observed in our recently reported amorphous B-P films by reactive sputtering.[21] This compositional flexibility is likely related to the ability of P to form homoelement bonds in the films and segregate as an elemental impurity. Hence, we assume that the excess P in CuP_{2+x} films with $x > 0$ is mainly bonded to other P atoms.

As-deposited CuP_{2+x} films did not exhibit any x-ray diffraction (XRD) peaks (Figure S2, Supporting Information), so we crystallized them in an RTA furnace at atmospheric pressure under a N_2 flow. Loss of phosphorus at moderate temperatures is a well-known phenomenon in many P-rich phosphides.[2] We also observed P losses in all our post-annealed CuP_2 films (Figs. 2(a,b)). However, the dependence of these P losses on the initial composition of the as-deposited films is not trivial.

In Fig. 2(a) we compare the P/Cu ratio before- and after annealing at 400 °C for 5 min for various initial compositions between $CuP_{1.3}$ and $CuP_{4.5}$. The P/Cu ratio is measured by x-ray fluorescence (XRF) so it represents an average through the depth of the film. Several interesting trends can be identified. First, thicker films generally experience milder P losses, since P located deeper in the film requires a longer time to diffuse out. Second, sufficiently thick films with initial composition in the $CuP_{2.2}$ – $CuP_{2.7}$ range can be "locked" into the desired CuP_2 stoichiometry by annealing (Fig. 2(b)). Third, films with severe P losses tend to approach the Cu_3P composition after annealing. Cu_3P is the most commonly reported binary stoichiometry in the Cu-P system.[5,6,27,28]

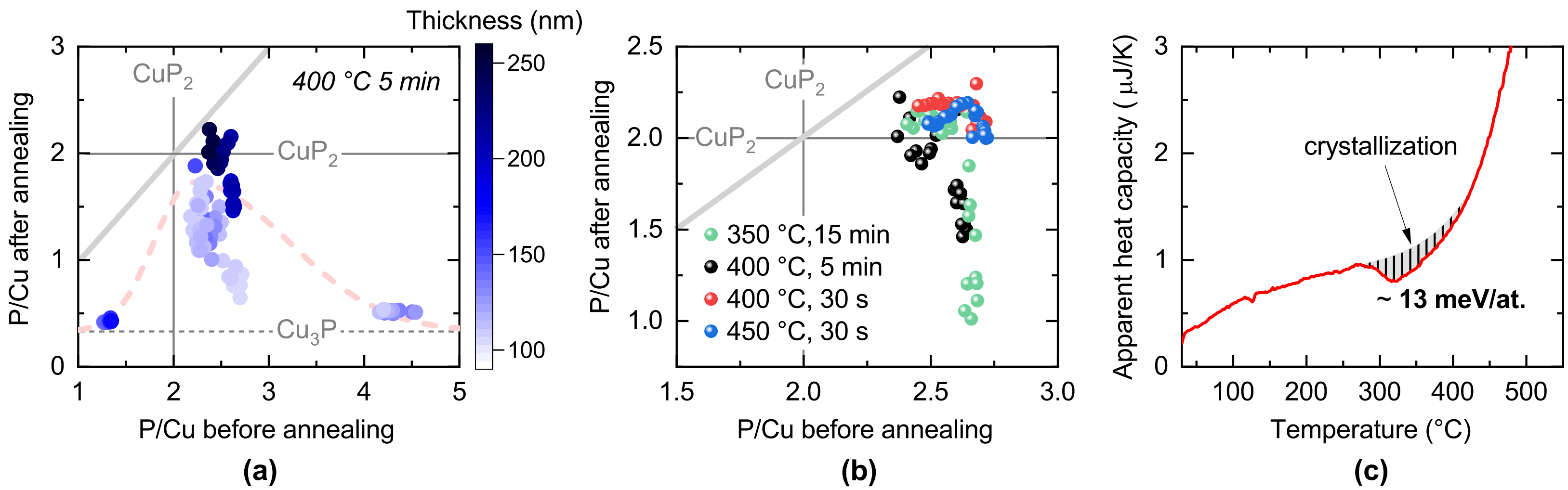

Figure 2: The effect of post-annealing on amorphous CuP_{2+x} films. (a): Change in P/Cu ratio after annealing for films of different initial compositions and thicknesses under constant annealing conditions (400 °C for 5 min). Vertical and horizontal lines indicate the CuP_2 and Cu_3P stoichiometries. The grey diagonal line corresponds to P/Cu ratios that are not modified by annealing. The dashed line is a guide to the eye, indicating that the films with initial composition closest to CuP_2 are the ones with least severe P losses. (b): Change in P/Cu ratio after annealing for films of $CuP_{2.4}$ – $CuP_{2.7}$ initial compostion and similar thicknesses under different annealing conditions. (c): Calorimetry experiment on an initially amorphous 90 nm-thick $CuP_{2.5}$ film deposited on a Si_3N_4 membrane. If we assume a baseline for the heat capacity as shown in the figure, the energy released in the 300 °C–400 °C region (area under the baseline) is estimated as 13 meV/atom.

Last, and most surprisingly, we find that highly P-rich initial compositions do *not* help achieve a higher P content in the post-annealed films. In fact the opposite is true. When the initial composition is in the (P-rich) $CuP_{4.1}$ – $CuP_{4.5}$ range, the post-annealed composition is around $CuP_{0.5}$ (Fig. 2(a)). When the initial composition is much poorer in P ($CuP_{1.3}$ – $CuP_{1.4}$ range) the post-annealed composition is similar, around $CuP_{0.4}$ (Fig. 2(a)). On the other hand, when the initial composition is in an intermediate $CuP_{2.2}$ – $CuP_{2.7}$ range closer to the desired CuP_2 stoichiometry, P losses upon annealing are much slower in films of comparable thickness.

Using these atomically dispersed precursors with moderate P excess with respect to the target CuP_2 stoichiometry, the necessary species for forming crystalline CuP_2 are readily available within a sub-nm distance of their ideal crystallographic site. This enables fast crystallization of monoclinic CuP_2. On the other hand, solid-state diffusion processes responsible for P losses have longer characteristic lengths, on the order of the film thickness (in our case, hundreds of nm). Thus, there is an optimal annealing time which is sufficient for CuP_2 to crystallize, but insufficient for substantial P losses to occur. Presumably, the lower total energy achieved by crystallizing the originally amorphous CuP_2 film (Fig. 2(c)) also helps delay P evaporation.

Conversely, precursor films that are too P-rich require solid-state diffusion to form a crystalline CuP_2 phase because Cu atoms are too far apart in the initial amorphous phase. This Cu diffusion process now competes with the unwanted P diffusion leading to P evaporation. As a result, P losses are much faster. These findings are summarized in the qualitative diagram shown in Fig. 3.

To visualize the P loss process, we image a film with final composition $CuP_{1.3}$ by scanning electron microscopy (SEM, Fig. 4). Two phases can be clearly distinguished on the micrometer scale: a porous polycrystalline matrix with grain size around 30 nm and islands of more compact morphology. The intensity ratio between the Cu and the P peaks in energy-dispersive x-ray spectroscopy (EDX) increases by a factor ~ 5.5 when moving from

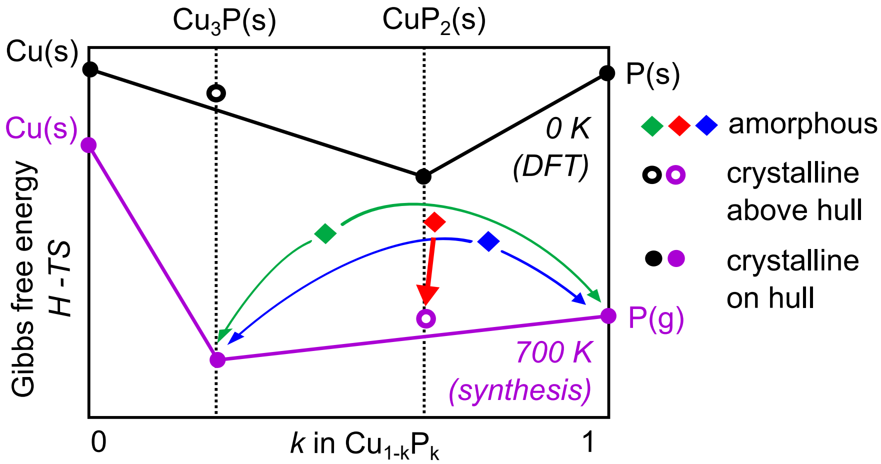

Figure 3: Qualitative convex hull of Cu-P system at two different temperatures. Among competing phases, only Cu_3P and the elements are considered. At 0 K, the Gibbs free energy only consists of enthalpy H, so the convex hull is drawn following DFT enthalpy calculations as available on the Materials Project database.[27] CuP_2 is found to be a stable phase (on the convex hull) and Cu_3P is slightly metastable (above the convex hull). At 700 K, our experiments indicate that CuP_2 is destabilized. Part of the reason may be a large entropic term TS for elemental P, which is in gaseous form at this temperature. When higher-energy amorphous precursors (diamond data points) are rapidly heated to 700 K, decomposition into Cu_3P and gaseous P is thermodynamically favored. However, CuP_2 formation is kinetically facilitated when the initial composition of the precursors is sufficiently close to the CuP_2 stoichiometry (red diamond).

the matrix to the islands (Fig. S1, Supporting Information). Thus, we conclude that the matrix consists of CuP_2 and the islands consist of Cu_3P. The mechanism of conversion from CuP_2 to Cu_3P appears to be diffusion of Cu in the plane of the substrate, contributing to the enlargement of seed Cu_3P islands. At the same time, P gradually evaporates elsewhere. Since the most stable gaseous form of phosphorus[29] at our annealing temperatures is P_4 and no intermediate solid phases between CuP_2 and Cu_3P are observed, the CuP_2 decomposition reaction can be written as $12\,CuP_2(s) \longrightarrow 4\,Cu_3P(s) + 5\,P_4(g)$.

Fig. 2(b) shows the effect of annealing temperature and time on the final composition. As expected, increasing the annealing time at fixed temperature results in more severe P losses (compare the data from 30 s versus 5 min annealing time at 400 °C). In general, longer annealing times can be tolerated at lower annealing temperatures. For example, annealing at 350 °C for 15 min yields about as many P-poor samples as the case of annealing at 400 °C for

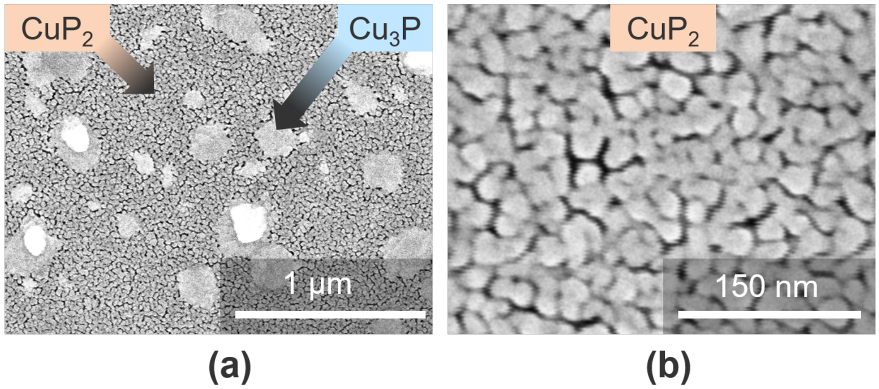

Figure 4: Morphology of a post-annealed film with overall $CuP_{1.3}$ composition. (a): Low-magnification SEM image showing a dual-phase morphology with a CuP_2 matrix and Cu_3P islands. (b): High-magnification SEM image showing porosity in the CuP_2 matrix. Phase identification was performed on the basis of spatially-resolved EDX spectra (Fig. S1, Supporting Information).

5 min. Note that the spread of final P/Cu ratios sometimes obtained for films of otherwise similar initial P/Cu ratios and thicknesses is mainly caused by the different positions of the samples inside the furnace. The samples located further downstream with respect to the gas flow tend to lose less P, possibly because they are exposed to a finite P partial pressure due to P evaporating from the samples further upstream.

We observe a decrease in the apparent heat capacity of an as-deposited $CuP_{2.5}$ film at around 300 °C by nanocalorimetry (Fig. 2(c)). This indicates an exothermic signal, which may be related to the transition from the amorphous to the (more stable) polycrystalline state. The heat capacity baseline needed to calculate the heat of crystallization is not straighforward to define. If we assume the baseline shown in Fig. 2(c), we estimate the crystallization energy of CuP_2 as 13 meV/atom. Although the uncertainty on this value is substantial, some qualitative conclusions can still be drawn. The calculated formation enthalpy of CuP_2 from the elements in their standard state is 112 meV/atom.[27] Since this value is much larger than the estimated crystallization energy, most of the formation energy has probably already been released during formation of the amorphous compound. The thermal energy of a solid at 400 °C is approximately $3kT = 174$ meV/atom using the Dulong-

Petit law. Thus, the extra stabilization achieved by crystallizing CuP_2 is only a small fraction of the thermal energy available at that temperature.

It is also interesting to consider typical values for the calculated energy difference between the most stable amorphous configuration and most stable crystalline polymorph for a given material. This quantity has been calculated in a previous study for 41 material systems (mainly oxides) at 0 K.[30] The energy difference varies between ~50 meV/atom and ~500 meV/atom depending on the material. The significantly lower crystallization energy measured in CuP_2 could indicate that the entropic contribution to the total energy is substantially higher in the amorphous state than in the crystalline state at finite temperatures. Higher entropy is indeed expected in the amorphous state due to higher disorder, and it would contribute to reducing the energy difference between the amorphous and crystalline state of CuP_2 at ~700 K with respect to 0 K. Although this explanation is plausible, it is also possible that CuP_2 and other non-oxide compounds simply exhibit different energetic trends than the computationally investigated selection of compounds. Computational analysis of the energetics of a more diverse range of amorphous material systems would certainly be useful.

Stability

Previous work on CuP_2 single crystals does not comment on their stability under ambient conditions. Based on simple observations on our thin-film samples, we suggest that the air stability of CuP_2 should be further investigated. A change in color is consistently observed in as-deposited CuP_{2+x} after few hours of exposure to ambient air, signaling a reaction that is not limited to a surface layer of a few nm thickness. For this reason, the films characterized in this work were annealed immediately after deposition. After annealing, the bulk properties of the films appear to be stable for a longer time (at least a few days) under ambient conditions, as judged by their visual appearance and electrical conductivity. The higher reactivity of amorphous CuP_{2+x} may be due to the extra P present before annealing and to the higher energy associated with the amorphous state (Fig. 2(c)). Both the amorphous and the polycrystalline films appear to be stable in a N_2 atmosphere.

After either type of film has been exposed to air for a sufficiently long time, the reaction front has reached the back surface of the film, as evident by visual inspection through the glass substrate. The exact details of the CuP_{2+x}-air reaction are currently unknown. However, XRF measurements reveal a large decrease in P/Cu ratio after prolonged exposure to air, indicating that the reaction involves P losses. We suspect that the high sputter pressure (2 Pa) necessary to obtain a P/Cu ratio above 2 in our growth setup may explain why the reaction of CuP_2 films with air is not limited to a surface layer. Films sputtered at high pressure are generally more porous and more air sensitive due to their higher surface area.[31] Thus, we cannot conclude that CuP_2 films are intrinsically unstable in air. The stability of CuP_2 films sputtered at lower pressures or deposited by other techniques should be investigated to clarify this issue.

Structural and vibrational properties

In agreement with nanocalorimetry results, the originally amorphous CuP_{2+x} films only begin to show crystalline XRD peaks above 300 °C annealing temperature (Fig. S2, Supporting Information). Beyond this lower limit, it is possible to obtain polycrystalline CuP_{2+x} films in the $P2_1/c$ structure under various annealing conditions. As long as the final composition is close to the nominal CuP_2 stoichiometry, XRD patterns of films processed under different annealing conditions are rather similar (Fig. S2, Supporting Information). As an example, the XRD pattern of a CuP_2 film annealed at 450 °C for 30 s (Fig. 5(a)) contains all the peaks expected for the $P2_1/c$ structure, without major preferential orientation effects and without clear peaks from secondary phases above the noise level. The XRD peak positions closely match the positions of the reference bulk CuP_2 sample,[7] indicating that structural parameters (including the short Cu-Cu distance) are about the same in thin-film and bulk CuP_2. XRD peaks from Cu_3P in the hexagonal $P6_3cm$ structure are observed in CuP_{2+x}

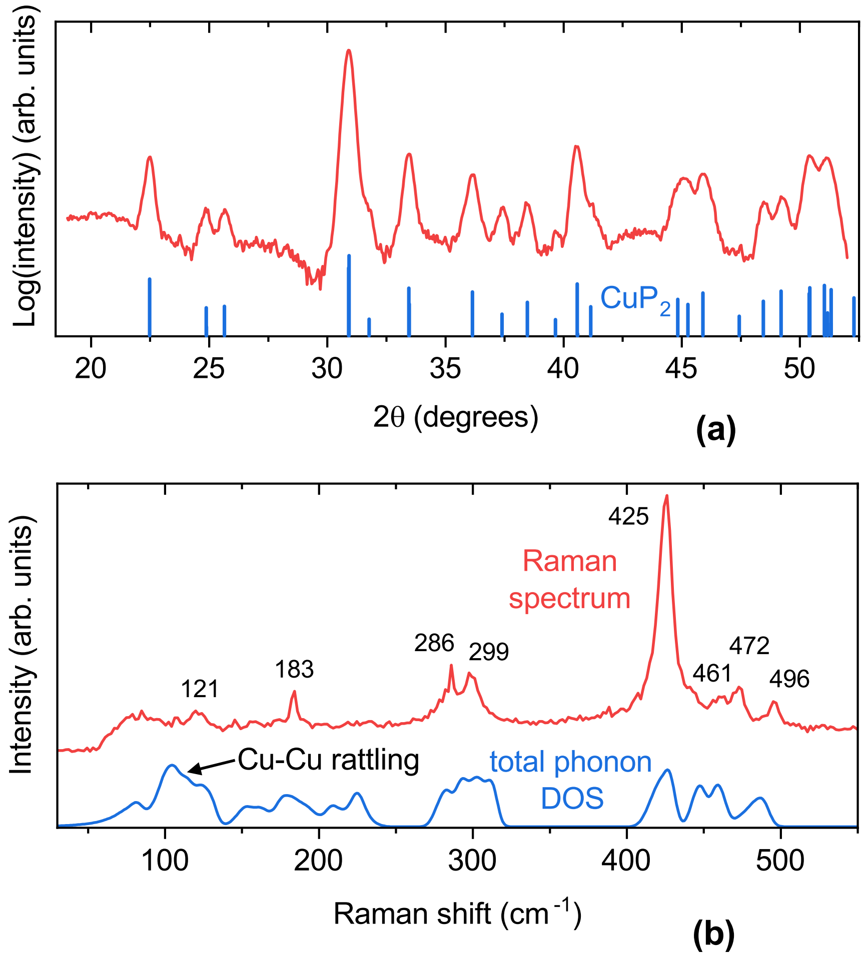

Figure 5: Structural and vibrational characterization of a film with CuP_2 stoichiometry after post-annealing at 450 °C for 30 s. (a): Experimental XRD pattern together with the reflections expected for randomly-oriented CuP_2 in the monoclinic $P2_1/c$ structure.[7] XRD patterns under other annealing conditions are shown in Fig. S2, Supporting Information. (b): Experimental Raman spectrum with labels for the identified peak positions. The total phonon density of states of CuP_2 in the $P2_1/c$ structure, as calculated in the Materials Project database,[27] is also shown. The Cu-Cu rattling mode ($\sim$100 cm^{-1}) believed to limit the thermal conductivity of CuP_2[26] is indicated.

films when $x < 0$ (Fig. S2, Supporting Information). However, the threshold value of x at which Cu_3P peaks begin to appear strongly varies with annealing conditions. When $x > 0$ (P-rich films), no XRD peaks associated with secondary phases like Cu_2P_7 or elemental phosphorus are observed up to the most P-rich composition reached in this study ($CuP_{2.2}$).

It might be tempting to conclude that single-phase CuP_{2+x} can be grown over a wide x range, in which defect formation is favored over secondary phase precipitation. However, secondary phases in amorphous form (not detected by XRD) are likely to be present in our samples for the following reasons. First, amorphous secondary phases were identified in a previous study on the phase equilibrium between Cu_3P and CuP_2 in powder form.[32] This observation rendered XRD-determined phase boundaries incorrect. Second, our short annealing times may not be sufficient to crystallize phases with a significantly different composition than the original precursors. In fact, Cu_3P can only form if CuP_2 loses more than 80% of its original P in some regions of the film. If the annealing process is stopped before these losses can take place, and if there are no stable phases between CuP_2 and Cu_3P, the likely result is formation of amorphous phases with intermediate composition. Third, the electrical conductivity of our films is roughly constant in the $CuP_{1.0}$ – $CuP_{2.2}$ composition range (Fig. 6(a)). It is improbable that the high defect densities required to accommodate this nonstoichiometry do not have any effect on the electrical properties. Thus, electrically inactive secondary phases (such as the disconnected Cu_3P islands shown in Fig. 4(a)) are very likely to coexist with point defects in highly nonstoichiometric CuP_2.

The Raman spectrum of the same sample used for XRD characterization is plotted in Fig. 5(b). The phonon density of states (DOS) of CuP_2, as calculated by density functional perturbation theory in good agreement with recent experiments,[26] is also shown for comparison.[27,33,34] Since Raman spectra of bulk CuP_2 are not available in the literature, we briefly discuss some qualitative aspects here. Raman features originating from the phonon bands centered around $300\,\mathrm{cm}^{-1}$ and $450\,\mathrm{cm}^{-1}$ can clearly be seen in the experimental spectrum. In particular, the most intense Raman peak at $425\,\mathrm{cm}^{-1}$ probably arises from one of the lowest-energy phonon branches within the highest-energy band in the calculated DOS. All modes in this band essentially involve vibrations of P atoms with nearly static Cu atoms. The lower the phonon energy, the larger the contribution from Cu vibrations, as expected from the larger mass of Cu.

Since the film is polycrystalline, there are selection rules for Raman-active phonon modes and the Raman spectrum will not directly reflect the phonon DOS. Specifically, all atoms in

CuP_2 are at 4e Wyckoff positions of the $P2_1/c$ space group, so only the A_g and B_g modes are Raman-active according to the character tables.[35] With a 12-atom unit cell, 18 Raman-active modes are predicted in total.[35] Eight peaks can be identified the experimental spectrum (Fig. 5(b)). The Cu-Cu rattling mode identified by Qi et al. as an important scatterer of heat-transporting phonons[26] is either symmetry-forbidden or too low in intensity to be distinguished by Raman spectroscopy.

Electrical and optical properties

The room-temperature electrical conductivity of post-annealed polycrystalline films in the $CuP_{2.0}$ – $CuP_{2.2}$ composition range is between 0.5 S/cm and 1.0 S/cm at room temperature, without a clear dependence on the P/Cu ratio (Fig. 6(a)). The conductivity generally increases with increasing annealing temperature, regardless of annealing time (Fig. S4, Supporting Information). Previously reported conductivites of CuP_2 single crystals range from 0.01 S/cm to 30 S/cm, presumably due to differences in the crystal quality.[6,8–10] Films with severe P losses have significantly higher conductivities (Fig. 6(a)), probably due to the presence of the highly conductive Cu_3P phase.[6] The Seebeck coefficient measured on a freshly annealed $CuP_{2.0}$ film is $(+390 \pm 10)\,\mu V/K$ (Fig. S3, Supporting Information), indicating native p-type doping. All previously reported CuP_2 single crystals were also p-type with higher Seebeck coefficients in the $690\,\mu V/K$–$820\,\mu V/K$ range. The work function, measured with a Kelvin probe in air on a freshly annealed $CuP_{2.0}$ film, is $(5.0 \pm 0.1)\,eV$.

CuP_2 is a relatively strong absorber of light. Its absorption coefficient α reaches $10^5\,cm^{-1}$ at a photon energy $h\nu = E_g + 0.6\,eV$ above its band gap $E_g = (1.5 \pm 0.1)\,eV$ (Fig. 6(b)). This compares favorably even with the most efficient direct gap photovoltaic absorbers such as GaAs, CdTe, and $CH_3NH_3PbI_3$ (MAPI).[36] In fact, the absorption coefficient is as high as in some exciton-enhanced photoabsorbers such as BiI_3 and Cu_2BaSnS_4,[37,38] indicating that CuP_2 may deserve more detailed optoelectronic characterization.

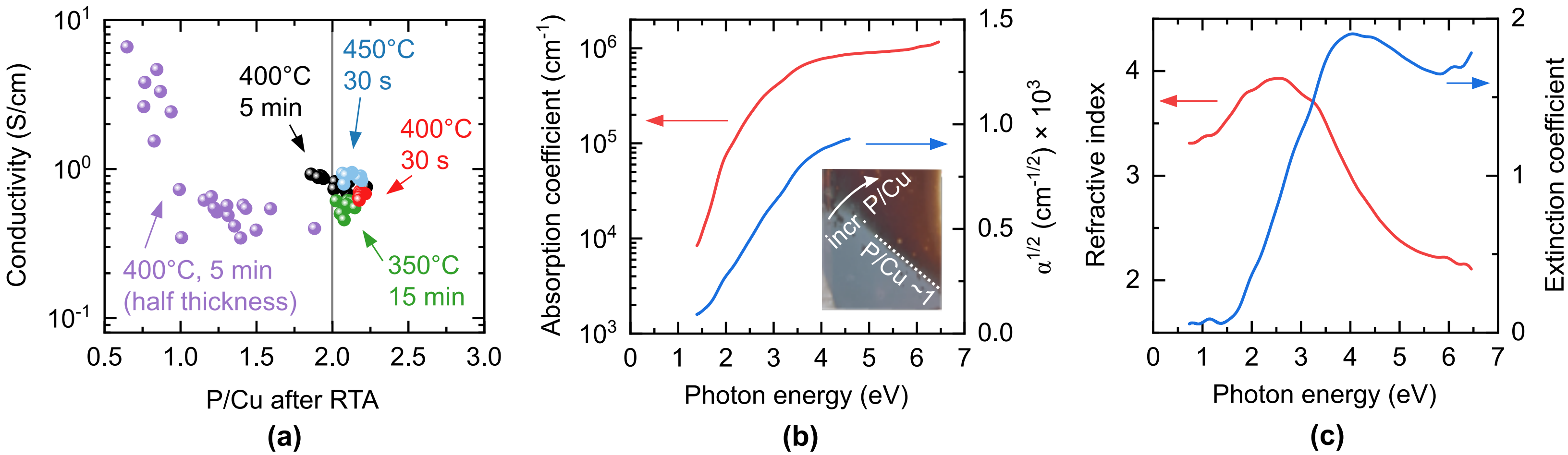

Figure 6: Room-temperature electrical and optical properties of post-annealed CuP_{2+x} films. (a): Electrical conductivity as a function of composition (measured after annealing) and annealing conditions. Films are of comparable thickness except for the P-poor purple data points, which have about half the thickness as the other ones. A zoomed-in view around the CuP_2 stoichiometry is available in Fig. S4, Supporting Information. (b): Absorption coefficient α of a post-annealed $CuP_{2.0}$ film together with a $\alpha^{1/2}$ plot versus photon energy. Inset of (b): Photograph of a film with increasing P/Cu ratio from bottom left to top right. When the P/Cu ratio decreases below roughly 1, the appearance of the film changes from dark red (characteristic of semiconducting CuP_2) to grey (characteristic of metallic Cu_3P). (c): Refractive index and extinction coefficient of the same $CuP_{2.0}$ film shown in (b).

We find that $\alpha^{1/2}$ is linear in photon energy over a 2 eV spectral range above the band gap (Fig. 6(b)), indicating that $\alpha \propto (h\nu - E_g)^2$. Both the estimated band gap and the spectral dependence of the absorption coefficient are in agreement with previous work on CuP_2 single crystals.[8–10] Because the $\alpha \propto (h\nu - E_g)^2$ behavior is often associated with an indirect gap in conventional semiconductors,[39] an indirect gap was previously assumed for these CuP_2 crystals.[8,10]

However, there are at least two other factors to consider. (1) The absorption strength of CuP_2 is high even for a direct gap material, so indirect transitions are unlikely to be responsible for it. (2) According to the calculated band structure of CuP_2,[27] the fundamental gap should be direct and located between the Γ and the Y point of the Brillouin zone. Two indirect gaps with slightly higher energies exist, due to additional valence band pockets at the X point and between the Y and H points.[27] Even though we observe a $\alpha \propto (h\nu - E_g)^2$ behavior, care should be taken when employing the absorption characteristics typical of Group IV and III-V semiconductors to interpret the nature of the optical transitions of other semiconductors with substantially different band structures. A clear difference between CuP_2 and conventional semiconductors is that the former has many valence- and conduction band pockets at different points of the Brillouin zone. Hence, many different optical transitions can contribute to the overall absorption coefficient. The refractive index of CuP_2 is 3.3–3.4 in the transparent region (Fig. 6(c)). Extrapolation of the real part of the dielectric function to zero photon energy (Fig. S5, Supporting Information) yields a high-frequency permittivity $\varepsilon_\infty = 10.5 \pm 1.0$. Interestingly, there seems to be a critical P/Cu ratio close to 1, where the electrical and optical properties shift from being "CuP_2-like" (semiconducting and IR-transparent) to being "Cu_3P-like" (metallic and opaque). This transition is manifested by an abrupt change in conductivity (Fig. 6(a)) and visual appearance (inset of Fig. 6(b)).

Thermoelectric characterization

We conducted DC and double AC Hall effect measurements, as well as temperature-dependent thermoelectric characterization of three films. They have the following compositions: $Cu_{2.50}P$ (labeled "$Cu_{3-z}P$"), $Cu_{1.61}P$, and $CuP_{1.35}$ (labeled "CuP_{2-y}"). We use these labels to emphasize similarity to Cu_3P and CuP_2 as discussed in the previous section. This set of films was deposited on Si_3N_4 membranes as part of a microchip-based thin-film transport characterization platform.[40] Differences between this set of films and the films deposited on glass characterized in the rest of the article are listed in the Supporting Information. Since these films have intermediate compositions between CuP_2 and Cu_3P, their properties may be influenced by inhomogeneity, as exemplified by the dual-phase morphology shown in Fig. 4. Nevertheless, important qualitative trends in the transport properties of these films as a function of composition can still be discerned.

The temperature dependence of the electrical conductivity (Fig. 7(a)) suggests that CuP_{2-y} is a nondegenerately doped semiconductor and that the two other films are either metallic or degenerately doped semiconductors. Hall effect measurements at room temperature confirm this interpretation (Fig. 8), with high carrier concentrations measured in $Cu_{3-z}P$ and $Cu_{1.61}P$ (above $10^{20}\,\mathrm{cm^{-3}}$) and a moderate carrier concentration measured in CuP_{2-y} ($10^{15}\,\mathrm{cm^{-3}}$–$10^{17}\,\mathrm{cm^{-3}}$). All films have a positive Hall voltage confirming their p-type conductivity. Note that the conductivity of $Cu_{1.61}P$ and CuP_{2-y} after one month of storage is appreciably lower (Fig. 7(a)), highlighting possible stability issues as discussed in the previous sections.

Due to the inverse relationship between carrier concentration and thermovoltage,[41] the Seebeck coefficient is highest in CuP_{2-y} and lowest in $Cu_{3-z}P$ (Fig. 7(b)). Interestingly, the Seebeck coefficient increases linearly with temperature in all three films (Fig. 7(b)). This behavior is often a sign of a temperature-independent carrier concentration,[41] a typical feature of materials with non-zero density of states at the Fermi level (i.e., metals and degenerate semiconductors such as $Cu_{3-z}P$ and $Cu_{1.61}P$). However, a linear increase of the Seebeck co-

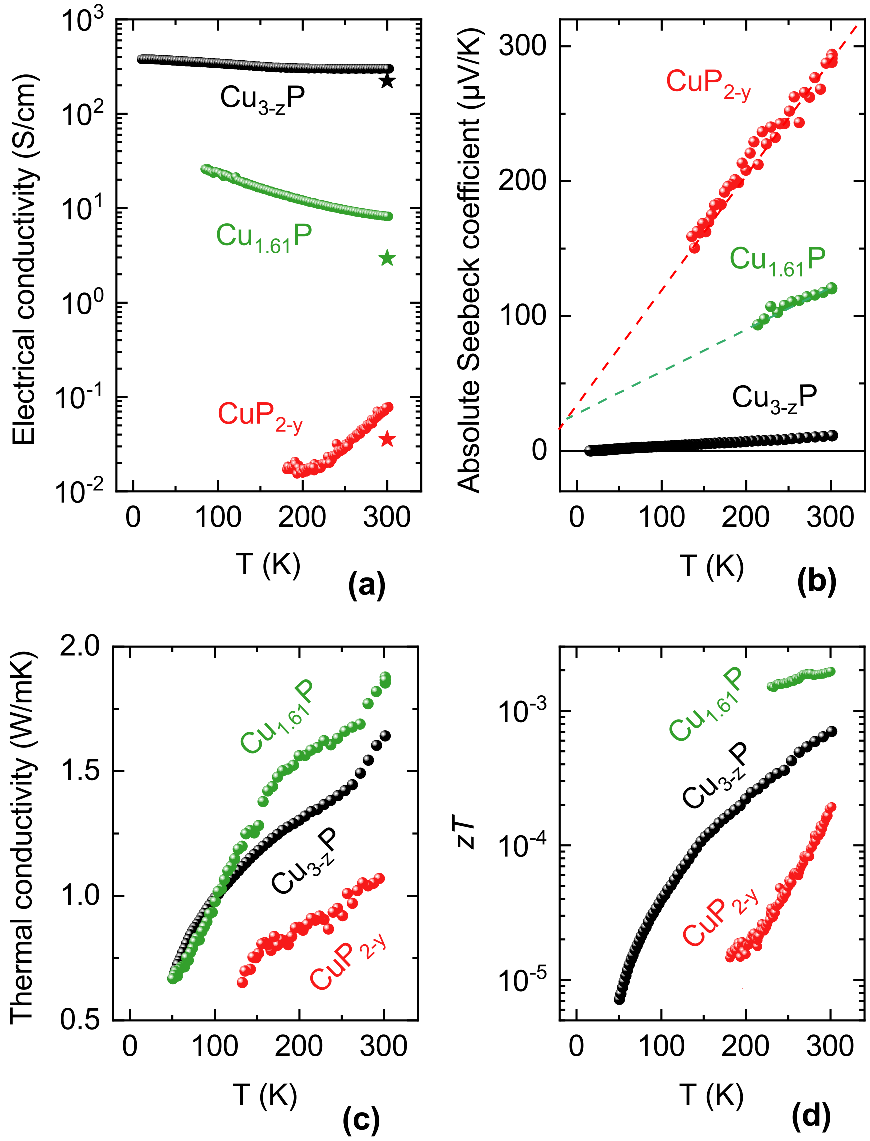

Figure 7: Thermoelectric properties of three post-annealed Cu-P films as a function of temperature T. The compositions after annealing are indicated following the labeling scheme from Sec. . (a): Electrical conductivity σ, which was also remeasured at room temperature one month after the temperature-dependent measurement (star markers). (b): Absolute Seebeck coefficients $S \equiv S_{\mathrm{Cu-P}}$, with linear trends indicated. (c): Thermal conductivity κ. (d): Thermoelectric figure of merit $zT = \sigma S^2 T/\kappa$.

efficient with temperature is not readily explained for a more weakly doped semiconductor like CuP_{2-y}. In an ideal scenario, we would expect the carrier concentration to increase with temperature due to increasing defect ionization, and the Seebeck coefficient to decrease accordingly. The reason for this discrepancy is unclear. One could invoke the role of film inhomogeneity due to the presence of Cu_3P secondary phases (Fig. 4), or assume that the increase of electrical conductivity with temperature (Fig. 7(a)) is due to mobility changes rather than to the hole concentration changes. Yet, a simultaneous increase in hole concentration and Seebeck coefficient with temperature was reported for CuP_2 single crystals,[8] where inhomogeneity effects can be excluded. Multi-band transport could also cause an unusual temperature behavior due to increasing contributions from the additional valence band pockets of CuP_2 with increasing temperature. However, application of the Boltzmann transport equation[42] on the calculated CuP_2 band structure[27] reveals that a significant decrease in the Seebeck coefficient is expected in the 200 K–300 K range assuming a concurrent increase in hole concentration by one order of magnitude (Fig. S6, Supporting Information).

As another hypothesis, one could assume that CuP_{2-y} is highly compensated by donor defects at low temperatures, but its p-type character becomes more dominant at higher temperatures due to activation of a deeper acceptor. If this hypothesis is correct, one would expect both the electrical conductivity and the Seebeck coefficient to increase with temperature as we experimentally observe – the former due to an increase in the concentration of ionized acceptors, the latter due to a decreasing contribution from the (negative) n-type Seebeck coefficient.[41] Previous work also suggested the possibility of charge compensation in CuP_2 single crystals based on the temperature dependence of their carrier mobility.[10] The position of the acceptor level in our CuP_{2-y} film can be estimated as (121 ± 3) meV above the valence band from an Arrhenius plot of the electrical conductivity in the 230 K–300 K temperature range (Fig. S7, Supporting Information).

The room-temperature thermal conductivity of CuP_{2-y} is 1.1 W/Km (Fig. 7(c)). This value is lower than in CuP_2 single crystals (3.6 W/Km–4.7 W/Km depending on lattice direction)[26] as may be expected for a polycrystalline sample. Our measured conductivity is, however, in excellent agreement with the calculated 1.12 W/Km amorphous limit for bulk CuP_2.[12] The increasing thermal conductivity with increasing temperature is unlike the $\propto 1/T$ behavior typical of crystalline semiconductors in this temperature range. Instead,

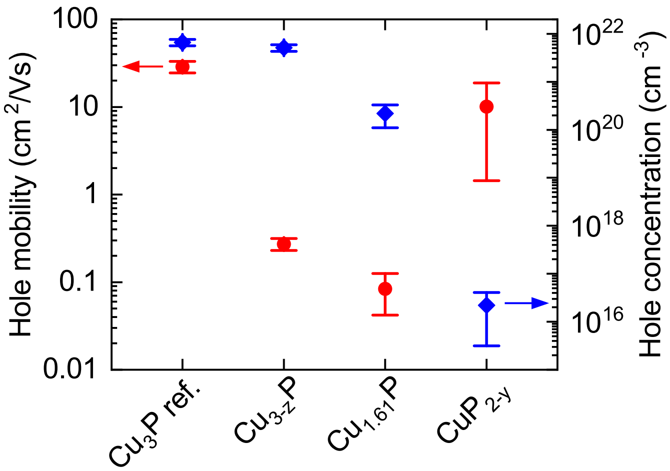

Figure 8: Hole mobility and concentration by double AC Hall effect measurements on the same Cu-P films shown in Fig. 7. The film labeled "Cu_3P ref." is a continuous polycrystalline Cu_3P film deposited by reactive sputtering at 360 °C and used as a reference.

it is often observed in amorphous or highly disordered materials, consistently with the observation that our measured conductivity is very close to the amorphous limit. Based on these results, we assume that the phonon mean free path in the CuP_{2-y} film is low due to disorder[43] and/or phonon boundary scattering.[44] The latter is likely enhanced by the small grains, low thickness, and porous morphology of the film.[43–45] The electronic contribution to the thermal conductivity is negligible due to the low hole concentration of CuP_{2-y} (Fig. 8). The thermal conductivities of $Cu_{3-z}P$ and $Cu_{1.61}P$ are only slightly higher and their temperature dependences are similar to the case of CuP_{2-y}. Thus, we conclude that the thermal conductivity is phonon-mediated and strongly limited by film morphology in all three films. In fact, scattering of charge carriers (holes) is also morphology-limited. The hole mobility of the present $Cu_{3-z}P$ film (0.27 cm^2/Vs) is two orders of magnitude lower than in a continuous Cu_3P film on glass with about the same carrier concentration (28.8 cm^2/Vs, see Fig. 8).

CuP_2 has recently been proposed as a potential thermoelectric material.[12,13] Our measurements on a CuP_{2-y} film confirm that the lattice contribution to its thermal conductivity is indeed sufficiently low for thermoelectric applications. However, the thermoelectric figure of merit zT at room temperature is still low for all investigated compositions (Fig 7(d)) due to low power factors (Fig S8, Supporting Information). In the vicinity of the Cu_3P stoichiom-

Table 1: List of electrical, optical, and thermal properties measured in this study on post-annealed CuP_{2+x} films at room temperature. The film composition is $CuP_{2.0}$ for all properties except for the thermal conductivity ($CuP_{1.35}$).

Electrical conductivity	0.5–1.0	S/cm
Seebeck coefficient	$+390 \pm 10$	μV/K
Thermal conductivity	1.1 ± 0.1	W/Km
Band gap	1.5 ± 0.1	eV
Work function	5.0 ± 0.1	eV
Dielectric constant (ε_∞)	10.5 ± 1.0	

etry, the main issue is a low Seebeck coefficient. In the vicinity of the CuP_2 stoichiometry, the main issue is low electrical conductivity. Even taking the more favorable properties of our CuP_2 films on glass (Table 1) or of previously reported CuP_2 single crystals[8] the zT value at room temperature would only be 0.004 and 0.05, respectively. It might be possible to optimize the hole concentration of CuP_2 by extrinsic doping to obtain higher zT values. Nevertheless, phosphorus losses at moderate temperatures and potential stability issues under ambient conditions are likely to limit its practical applicability in thermoelectric devices. Similar issues might exist in other phosphorus-rich phosphides.

Conclusion

We deposited amorphous CuP_{2+x} thin films with a wide range of x (positive and negative) by reactive sputtering in a PH_3/Ar atmosphere. Either a metallic Cu target or a compound Cu_3P target can be used as a deposition source. Some of the amorphous CuP_{2+x} films could be converted to polycrystalline CuP_2 by rapid thermal annealing in an inert atmosphere at 1 bar. Three conditions must be satisfied to do so: (i) short annealing times, (ii) moderate annealing temperatures in the 350 °C–450 °C range, and (iii) initial composition sufficiently close to the ideal CuP_2 stoichiometry. Remarkably, amorphous films that were either too P-poor *or too P-rich* quickly decomposed into Cu_3P and gaseous phosphorus upon heating. This “compositional lock-in" behavior highlights the importance of pre-existing short-range order for kinetic stabilization of materials under conditions where decomposition and crystallization are in competition with each other.

Polycrystalline CuP_{2+x} films are semiconductors with native p-type conductivity. Their electrical properties are rather insensitive to elemental composition in the vicinity of the stoichiometric point, and only moderately affected by the annealing conditions. The thermal conductivity of a P-poor CuP_2 film is 1.1 W/Km at room temperature, confirming its potential applicability as a thermoelectric material. However, the hole conductivity of CuP_2 is too low to achieve a high power factor (and therefore a high zT value) without extrinsic doping. Furthermore, decomposition of CuP_2 into Cu_3P and gaseous phosphorus at around 400 °C hinders high-temperature applications. Although stability issues are not mentioned in the CuP_2 single-crystal literature, our polycrystalline CuP_{2+x} films were only stable in ambient conditions for a few days. It is currently not clear if this issue is related to the porous morphology of our films, or if it is an intrinsic behavior of CuP_2.

Finally, CuP_2 is a stronger light absorber than many established photovoltaic materials, with absorption coefficient rapidly rising to $10^5\,\mathrm{cm}^{-1}$ above its 1.5 eV band gap. Combined with a native doping density in the optimal range for a photovoltaic absorber in a pn junction solar cell ($10^{15}\,\mathrm{cm}^{-3}$–$10^{17}\,\mathrm{cm}^{-3}$), we conclude that CuP_2 may deserve more detailed optoelectronic characterization.

Experimental details

Film growth

Amorphous CuP_{2+x} thin films were deposited on Corning Eagle XG borosilicate glass by reactive radio-frequency (RF) sputtering over a $10 \times 5\,\mathrm{cm}^2$ area. A Cu target and a Cu_3P target were co-sputtered at 2 Pa total pressure in a 5% PH_3/Ar atmosphere without intentional heating and without substrate rotation. The targets were oriented so that one short side of the substrate would mainly be coated by the Cu target and the other short side by the Cu_3P target.

Immediately after deposition, CuP_{2+x} films were cut into smaller pieces and annealed in a lamp-based rapid thermal annealing (RTA) furnace in a N_2 atmosphere. Because of the sputtering target geometry and differences in their applied power, small gradients in P/Cu ratio and film thickness were obtained across the substrate. These gradients enabled us to characterize several data points ("samples") for each annealing run, each with a distinct composition and thickness. More details on film deposition and annealing are available in the Supporting Information.

Film characterization

All measurements except for nanocalorimetry and thermoelectric/Hall effect characterization were performed within 24 h after annealing to avoid sample degradation. The combinatorial characterization data arising from compositional gradients in the films was managed with the COMBIgor tool,[46] the Research Data Infrastructure,[47] and integrated into the High-Throughput Experimental Materials Database.[48]

Elemental composition and film thickness were determined by x-ray fluorescence (XRF) calibrated by Rutherford backscattering spectrometry (RBS, composition) and spectroscopic ellipsometry (thickness). X-ray diffraction (XRD) measurements were conducted using Cu K_α radiation, a 2D detector, and a fixed incidence angle of 10°. Raman spectra were measured with 532 nm excitation wavelength and 4 W/mm^2 power density. Scanning electron microscopy (SEM) images were taken at 5 kV beam voltage.

Sheet resistance was measured with a collinear four-point probe directly contacting the film. The Seebeck coefficient of a CuP_2 film on glass was measured in a custom-built setup using In contacts. The work function was measured with a Kelvin probe calibrated with a standard Au sample. Absorption coefficient and optical functions were extracted by spectroscopic ellipsometry. Due to higher porosity in the upper part of the film, we modeled the system as a glass substrate of known optical functions, a CuP_2 layer with a linearly increasing fraction of air from bottom to top,[49] and a roughness layer treated with Bruggeman effective medium theory.

For nanocalorimetry and thermoelectric/Hall effect characterization, CuP_{2+x} films were deposited on previously described microfabricated chips designed for calorimetry[50] and in-plane thermoelectric characterization[40] of thin-film samples. In both types of chips, CuP_{2+x} was deposited on a free-standing Si_3N_4 membrane. Due to the fragility of the membrane, thinner CuP_{2+x} films (90 nm–120 nm) were employed for these studies.

Nanocalorimetry experiments were conducted in a N_2 atmosphere on an as-deposited amorphous film with initial $CuP_{2.5}$ composition, with an average heating rate of roughly 5000 °C/s. Temperature-dependent thermoelectric characterization (electrical and thermal conductivity and Seebeck coefficient) was performed in vacuum on three films with different compositions after annealing. The electrical conductivity was measured using the van der Pauw (vdP) method[51] The Seebeck coefficient was measured with respect to platinum metals lines using an internal four-probe platinum thermometer.[40] The thermal conductivity was derived from the current-voltage characteristics of membrane heaters/thermometers in the self-heating regime.[40,52] The hole concentration and mobility were measured on the same samples by double AC Hall.[53] More details on all measurements are available in the Supporting Information.

Supporting Information

EDX analysis of a multiphase film, XRD patterns as a function of composition and annealing conditions, electrical conductivity close to the ideal CuP_2 stoichiometry, complex dielectric function spectra, RBS spectra used for calibration of elemental composition, simulation of Seebeck coefficient of CuP_2, additional thermoelectric characterization data.

Acknowledgements

This project has received funding from the European Union's Horizon 2020 research and innovation programme under the Marie Sklodowska-Curie grant agreement No 840751 (synthesis work and most characterization and analysis work). This work was authored in part at the National Renewable Energy Laboratory, operated by Alliance for Sustainable Energy, LLC, for the U.S. Department of Energy (DOE) under Contract No. DE-AC36-08GO28308. Funding supporting development and operation of synthesis and characterization equipment was provided by the Office of Science, Office of Basic Energy Sciences. The authors gratefully acknowledge support of the Helmholtz Energy Materials Foundry (HEMF). Certain commercial equipment, instruments, or materials are identified in this document. Such identification does not imply recommendation or endorsement by the National Institute of Standards and Technology (NIST), nor does it imply that the products identified are necessarily the best available for the purpose. Nanocalorimeter fabrication was performed in part at the NIST Center for Nanoscale Science & Technology (CNST).

References

(1) Pöttgen, R.; Hönle, W.; von Schnering, H. G. *Encyclopedia of Inorganic and Bioinorganic Chemistry*; John Wiley and Sons, Ltd: Chichester, UK, 2011.

(2) Corbridge, D. E. C. *Phosphorus : chemistry, biochemistry and technology*, 6th ed.; CRC Press, 2013; p 608.

(3) Samuel, V.; Rao, V. J. Optical and valence band studies of ZnP_2 thin films. *Journal of Materials Research* **1989**, *4*, 185–188.

(4) Denis, V. A.; Sheleg, A. U.; Unyarkha, L. S. Crystallization kinetics and phase transformations of zinc- and cadmium diphosphide films. *Crystal Research and Technology* **1989**, *24*, 585–590.

(5) Haraldsen, H. Beiträge zur systematischen Verwandtschaftslehre. 87. Über die Phosphide des Kupfers. *Zeitschrift für anorganische und allgemeine Chemie* **1939**, *240*, 337–354.

(6) Juza, R.; Bär, K. Leiter und Halbleiter unter den Phosphiden der ersten und zweiten Nebengruppe. *Zeitschrift für anorganische und allgemeine Chemie* **1956**, *283*, 230–245.

(7) Olofsson, O. The Crystal Structures of CuP_2 and AgP_2 with some Phase Analytical Data of the Cu-P and Ag-P Systems. *Acta Chemica Scandinavica* **1965**, *19*, 229–241.

(8) Goryunova, N. A.; Orlov, V. M.; Sokolova, V. I.; Shpenkov, G. P.; Tsvetkova, E. V. Preparation and some properties of CuP_2 single crystals. *Physica Status Solidi (b)* **1968**, *25*, 513–519.

(9) Odile, J. P.; Soled, S.; Castro, C. A.; Wold, A. Crystal growth and characterization of the transition-metal phosphides copper diphosphide, nickel diphosphide, and rhodium triphosphide. *Inorganic Chemistry* **1978**, *17*, 283–286.

(10) Kloc, C.; Lux-Steiner, M.; Keil, M.; Baumann, J.; Döll, G.; Bucher, E. Growth and characterization of CuP_2 single crystals. *Journal of Crystal Growth* **1990**, *106*, 635–642.

(11) von Känel, H.; Gantert, L.; Hauger, R.; Wachter, P. Photoelectrochemical production of hydrogen from p-type transition metal phosphides. *International Journal of Hydrogen Energy* **1985**, *10*, 821–827.

(12) Pöhls, J.-H.; Faghaninia, A.; Petretto, G.; Aydemir, U.; Ricci, F.; Li, G.; Wood, M.; Ohno, S.; Hautier, G.; Snyder, G. J.; Rignanese, G.-M.; Jain, A.; White, M. A. Metal phosphides as potential thermoelectric materials. *Journal of Materials Chemistry C* **2017**, *5*, 12441–12456.

(13) Jong, U.-G.; Ri, C.-H.; Pak, C.-J.; Kim, C.-H.; Cottenier, S.; Yu, C.-J. Metal phosphide

CuP_2 as a promising thermoelectric material: an insight from a first-principles study. *New Journal of Chemistry* **2021**, *45*, 21569–21576.

(14) Riyajuddin, S.; Azmi, K.; Pahuja, M.; Kumar, S.; Maruyama, T.; Bera, C.; Ghosh, K. Super-Hydrophilic Hierarchical Ni-Foam-Graphene-Carbon Nanotubes-Ni_2P–CuP_2 Nano-Architecture as Efficient Electrocatalyst for Overall Water Splitting. *ACS Nano* **2021**, *15*, 5586–5599.

(15) Kim, S.-O.; Manthiram, A. Phosphorus-Rich CuP_2 Embedded in Carbon Matrix as a High-Performance Anode for Lithium-Ion Batteries. *ACS Applied Materials and Interfaces* **2017**, *9*, 16221–16227.

(16) Harper, A. F.; Evans, M. L.; Morris, A. J. Computational Investigation of Copper Phosphides as Conversion Anodes for Lithium-Ion Batteries. *Chemistry of Materials* **2020**, *32*, 6629–6639.

(17) Liu, Z.; Yang, S.; Sun, B.; Yang, P.; Zheng, J.; Li, X. Low-Temperature Synthesis of Honeycomb CuP_2@C in Molten $ZnCl_2$ Salt for High-Performance Lithium Ion Batteries. *Angewandte Chemie International Edition* **2020**, *59*, 1975–1979.

(18) Chen, S.; Wu, F.; Shen, L.; Huang, Y.; Sinha, S. K.; Srot, V.; van Aken, P. A.; Maier, J.; Yu, Y. Cross-Linking Hollow Carbon Sheet Encapsulated CuP_2 Nanocomposites for High Energy Density Sodium-Ion Batteries. *ACS Nano* **2018**, *12*, 7018–7027.

(19) Zhang, Y.; Wang, G.; Wang, L.; Tang, L.; Zhu, M.; Wu, C.; Dou, S.-X.; Wu, M. Graphene-Encapsulated CuP_2: A Promising Anode Material with High Reversible Capacity and Superior Rate-Performance for Sodium-Ion Batteries. *Nano Letters* **2019**, *19*, 2575–2582.

(20) Schnepf, R. R.; Crovetto, A.; Gorai, P.; Park, A.; Holtz, M.; Heinselman, K. N.; Bauers, S. R.; Brooks Tellekamp, M.; Zakutayev, A.; Greenaway, A. L.; Toberer, E. S.;

Tamboli, A. C. Reactive phosphine combinatorial co-sputtering of cation disordered $ZnGeP_2$ films. *Journal of Materials Chemistry C* **2022**, *10*, 870–879.

(21) Crovetto, A.; Adamczyk, J. M.; Schnepf, R. R.; Perkins, C. L.; Hempel, H.; Bauers, S. R.; Toberer, E. S.; Tamboli, A. C.; Unold, T.; Zakutayev, A. Boron Phosphide Films by Reactive Sputtering: Searching for a P-Type Transparent Conductor. *Advanced Materials Interfaces* **2022**, *9*, 2200031.

(22) Willis, J.; Brabic, I.; Schnepf, R.; Heinselman, K.; Monserrat, B.; Unold, T.; Zakutayev, A.; Scanlon, D. O.; Crovetto, A. Prediction and realisation of high mobility and degenerate p-type conductivity in CaCuP thin films. *Chemical Science* **2022**, https://doi.org/10.1039/D2SC01538B.

(23) Momma, K.; Izumi, F. VESTA 3 for three-dimensional visualization of crystal, volumetric and morphology data. *Journal of Applied Crystallography* **2011**, *44*, 1272–1276.

(24) Pearson, W. B. The crystal structures of semiconductors and a general valence rule. *Acta Crystallographica* **1964**, *17*, 1–15.

(25) Pauling, L.; Kamb, B. A revised set of values of single-bond radii derived from the observed interatomic distances in metals by correction for bond number and resonance energy. *Proceedings of the National Academy of Sciences* **1986**, *83*, 3569–3571 .

(26) Qi, J. et al. Dimer rattling mode induced low thermal conductivity in an excellent acoustic conductor. *Nature Communications* **2020**, *11*, 5197.

(27) Jain, A.; Ong, S. P.; Hautier, G.; Chen, W.; Richards, W. D.; Dacek, S.; Cholia, S.; Gunter, D.; Skinner, D.; Ceder, G.; Persson, K. A. Commentary: The Materials Project: A materials genome approach to accelerating materials innovation. *APL Materials* **2013**, *1*, 011002.

(28) Rachkov, A. G.; Schimpf, A. M. Colloidal Synthesis of Tunable Copper Phosphide Nanocrystals. *Chemistry of Materials* **2021**, *33*, 1394–1406.

(29) Bock, H.; Mueller, H. Gas-phase reactions. 44. The phosphorus $P_4 \rightleftarrows 2P_2$ equilibrium visualized. *Inorganic Chemistry* **1984**, *23*, 4365–4368 .

(30) Aykol, M.; Dwaraknath, S. S.; Sun, W.; Persson, K. A. Thermodynamic limit for synthesis of metastable inorganic materials. *Science Advances* **2018**, *4*, eaaq0148.

(31) Crovetto, A.; Ottsen, T. S.; Stamate, E.; Kjær, D.; Schou, J.; Hansen, O. On performance limitations and property correlations of Al-doped ZnO deposited by radio-frequency sputtering. *Journal of Physics D: Applied Physics* **2016**, *49*, 295101.

(32) Wolff, A.; Pallmann, J.; Boucher, R.; Weiz, A.; Brunner, E.; Doert, T.; Ruck, M. Resource-Efficient High-Yield Ionothermal Synthesis of Microcrystalline $Cu_{3-x}P$. *Inorganic Chemistry* **2016**, *55*, 8844–8851 .

(33) Ong, S. P.; Cholia, S.; Jain, A.; Brafman, M.; Gunter, D.; Ceder, G.; Persson, K. A. The Materials Application Programming Interface (API): A simple, flexible and efficient API for materials data based on REpresentational State Transfer (REST) principles. *Computational Materials Science* **2015**, *97*, 209–215.

(34) Petretto, G.; Dwaraknath, S.; P.C. Miranda, H.; Winston, D.; Giantomassi, M.; van Setten, M. J.; Gonze, X.; Persson, K. A.; Hautier, G.; Rignanese, G.-M. High-throughput density-functional perturbation theory phonons for inorganic materials. *Scientific Data* **2018**, *5*, 180065.

(35) Kroumova, E.; Aroyo, M.; Perez-Mato, J.; Kirov, A.; Capillas, C.; Ivantchev, S.; Wondratschek, H. Bilbao Crystallographic Server : Useful Databases and Tools for Phase-Transition Studies. *Phase Transitions* **2003**, *76*, 155–170.

(36) Nishigaki, Y.; Nagai, T.; Nishiwaki, M.; Aizawa, T.; Kozawa, M.; Hanzawa, K.; Kato, Y.; Sai, H.; Hiramatsu, H.; Hosono, H.; Fujiwara, H. Extraordinary Strong Band-Edge Absorption in Distorted Chalcogenide Perovskites. *Solar RRL* **2020**, *4*, 1900555.

(37) Crovetto, A.; Hajijafarassar, A.; Hansen, O.; Seger, B.; Chorkendorff, I.; Vesborg, P. C. K. Parallel Evaluation of the BiI_3 , BiOI, and Ag_3BiI_6 Layered Photoabsorbers. *Chemistry of Materials* **2020**, *32*, 3385–3395.

(38) Crovetto, A.; Xing, Z.; Fischer, M.; Nielsen, R.; Savory, C. N.; Rindzevicius, T.; Stenger, N.; Scanlon, D. O.; Chorkendorff, I.; Vesborg, P. C. K. Experimental and First-Principles Spectroscopy of Cu_2SrSnS_4 and Cu_2BaSnS_4 Photoabsorbers. *ACS Applied Materials and Interfaces* **2020**, *12*, 50446–50454.

(39) Yu, P. Y.; Cardona, M. *Fundamentals of Semiconductors*; Graduate Texts in Physics; Springer Berlin Heidelberg: Berlin, Heidelberg, 2010.

(40) Linseis, V.; Völklein, F.; Reith, H.; Nielsch, K.; Woias, P. Advanced platform for the in-plane ZT measurement of thin films. *Review of Scientific Instruments* **2018**, *89*, 015110.

(41) May, A. F.; Snyder, G. J. In *Thermoelectrics and its Energy Harvesting*; Rowe, D. M., Ed.; CRC Press, 2012; Chapter 11.

(42) Madsen, G. K.; Carrete, J.; Verstraete, M. J. BoltzTraP2, a program for interpolating band structures and calculating semi-classical transport coefficients. *Computer Physics Communications* **2018**, *231*, 140–145.

(43) Cahill, D. G.; Pohl, R. O. Lattice Vibrations and Heat Transport in Crystals and Glasses. *Annual Review of Physical Chemistry* **1988**, *39*, 93–121.

(44) Liu, W.; Asheghi, M. Thermal Conductivity Measurements of Ultra-Thin Single Crystal Silicon Layers. *Journal of Heat Transfer* **2006**, *128*, 75–83.

(45) Kojda, D.; Hofmann, T.; Gostkowska-Lekner, N.; Habicht, K. Characterization and modeling of the temperature-dependent thermal conductivity in sintered porous silicon-aluminum nanomaterials. *Nano Research* **2022**, 1–8.

(46) Talley, K. R.; Bauers, S. R.; Melamed, C. L.; Papac, M. C.; Heinselman, K. N.; Khan, I.; Roberts, D. M.; Jacobson, V.; Mis, A.; Brennecka, G. L.; Perkins, J. D.; Zakutayev, A. COMBIgor: Data-Analysis Package for Combinatorial Materials Science. *ACS Combinatorial Science* **2019**, *21*, 537–547.

(47) Talley, K. R.; White, R.; Wunder, N.; Eash, M.; Schwarting, M.; Evenson, D.; Perkins, J. D.; Tumas, W.; Munch, K.; Phillips, C.; Zakutayev, A. Research data infrastructure for high-throughput experimental materials science. *Patterns* **2021**, *2*, 100373.

(48) Zakutayev, A.; Wunder, N.; Schwarting, M.; Perkins, J. D.; White, R.; Munch, K.; Tumas, W.; Phillips, C. An open experimental database for exploring inorganic materials. *Scientific Data* **2018**, *5*, 180053.

(49) Crovetto, A.; Cazzaniga, A.; Ettlinger, R. B.; Schou, J.; Hansen, O. Large process-dependent variations in band alignment and interface band gaps of Cu_2ZnSnS_4/CdS solar cells. *Solar Energy Materials and Solar Cells* **2018**, *187*, 233–240.

(50) Yi, F.; LaVan, D. A. Nanocalorimetry: Exploring materials faster and smaller. *Applied Physics Reviews* **2019**, *6*, 031302.

(51) van der Pauw, L. J. A method of measuring specific resistivity and Hall effect of discs of arbitrary shape. *Philips Research Reports* **1958**, *13*, 1–9.

(52) Völklein, F.; Reith, H.; Meier, A. Measuring methods for the investigation of in-plane and cross-plane thermal conductivity of thin films. *physica status solidi (a)* **2013**, *210*, 106–118.

(53) Kasai, A.; Abdulla, A.; Watanabe, T.; Takenaga, M. Highly Sensitive Precise Double AC Hall Effect Apparatus for Wide Resistance Range. *Japanese Journal of Applied Physics* **1994**, *33*, 4137–4145.

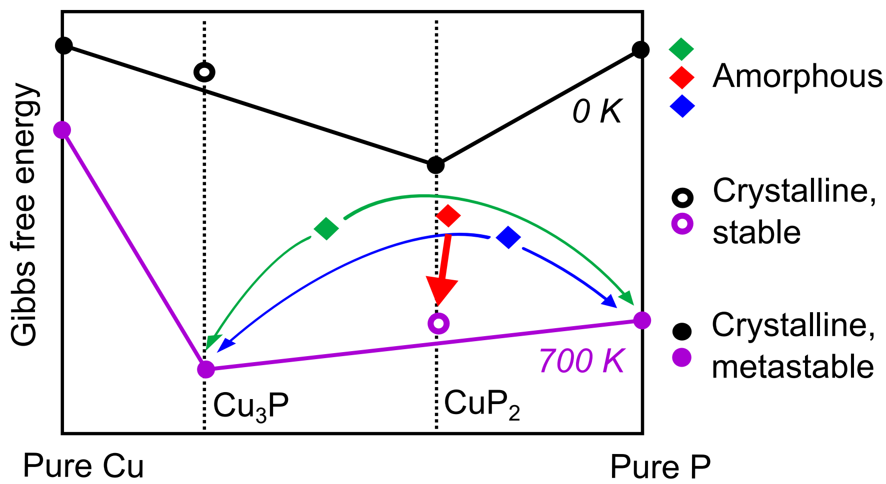

Table of content graphic